Superlattices in van der Waals materials: a low-energy electron microscopy study

Jong, T.A. de

8

CHARGE DENSITY WAVES IN MIXED POLYTYPE TaS_2

In this chapter the interaction between polytypes and charge density waves in TaS_2, a transition metal dichalcogenide, is studied. First, these concepts are each introduced. After reference experiments on pristine 1T-TaS_2, mixed polytypes are introduced and we show they can be distinguished from each other using the observed LEEM spectra. Using dark field LEEM and μLEED, charge density wave states are observed in the mixed polytypes. A mixed orientation, twinned commensurate charge density wave state consisting of in-plane orientational domains is observed. Here, a varying exact orientation of the CDW is tentatively connected to the domain size.

8.1 INTRODUCTION

8.1.1 TRANSITION METAL DICHALCOGENIDES

Transition metal dichalcogenides (TMDs) are a class of materials consisting of layers of transition metal atoms, sandwiched between two layers of chalcogen atoms (S, Se, Te), giving rise to metal dichalcogenide trilayers. The chalcogens are bonded to the metal by strong bonds, that vary in character from covalent to ionic, depending on the specific combination of the metal and chalcogen [211]. However, subsequent chalcogenide layers are only bonded by much weaker van der Waals interactions. This means that TMDs are van der Waals materials, which can be exfoliated into atomic layers, like graphene and hBN (although the thinnest possible 'atomic' layer for TMDs actually consists of three layers of atoms). It also means that these materials are intrinsically 2D-like, with the direction perpendicular to the layers (typically called the c-axis) different from the in-plane directions (a-axis, or, if needed $\mathbf{a}_0$- and $\mathbf{a}_1$-axis).

8.1.2 POLYTYPISM

Each layer of either metal or chalcogen atoms in TMDs is arranged in a trigonal lattice and occupies one of three sublattices, denoted a,b or c. In general, the atoms within a TMD layer can be arranged in one of two forms: Either the chalcogens are situated directly above each other, resulting in a prismatic (Pr) or '2H-like' layer, or the chalcogens are on two different sublattice sites, resulting in an octahedral (Oc) or '1T-like' layer, as shown in Figure 8.1.

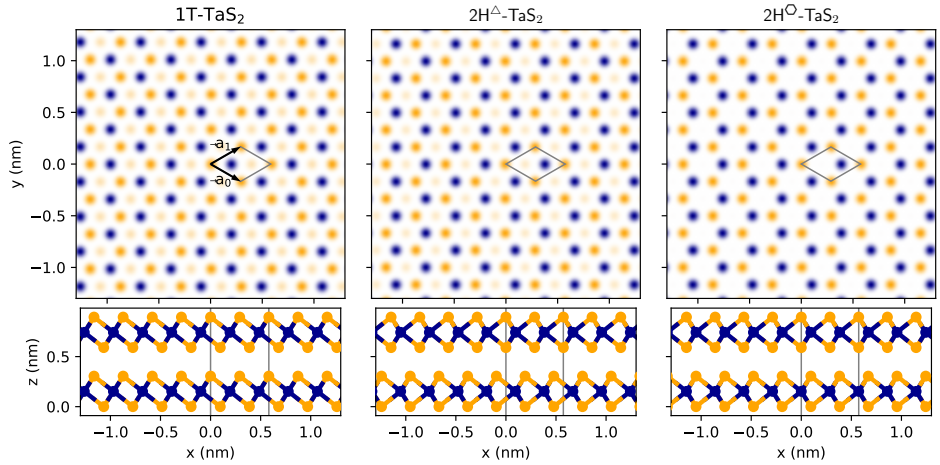

Figure 8.1: *Top and side view of the atomic structure of polytypes occurring in TaS_2. Sulfur atoms are depicted in yellow, tantalum atoms in dark blue. The 1T polytype (left) has an octahedral (Oc) arrangement of the sulfurs and a 1-layer unit cell. The 2H polytypes (center and right) have a prismatic (Pr) arrangement and a 2-layer unit cell. Unlike in MoS_2, in 2H-TaS_2, the bulk polytype is $2H^{\triangle}$ with the tantalum atoms directly on top of each other, although $2H^{\hexagon}$ might occur in mixed stackings.*

By stacking these two building blocks in different order and rotations, different bulk

polytypes are formed: lattice structures with the same atoms in it, but in different relative positions. Stacking octahedral layers results in the 1T polytype (where the "T" signifies a trigonal unit cell, and the "1" signifies a single van der Waals layer in that unit cell), stacking prismatic layers in the same orientation results in the 3R polytype (3 vdW layers in the rhombohedral unit cell), stacking prismatic layers in alternating orientations results in the 2H polytype (2 vdW layers in a hexagonal unit cell). Notably, depending on the exact TMD, two different stackings exist, both designated '2H' in literature. Both tantalum and niobium based TMDs occur in a stable bulk polytype with a (aba cbc) stacking, with the metal atoms in the same sublattice, which we will denote $2H^{\triangle}$ in this work, as all three of the trigonal sublattices are occupied. On the other hand, $Mo(S,Se,Te)_2$ and W based TMDs occur in a (aba bab) stacking, which we will here denote $2H^{\hexagon}$, as from a top-view atoms occur in hexagons [212]. For some TMDs, more complicated bulk polytypes, consisting of a mixture of layer types, are reported, e.g. $4H_a$ and $4H_b$ in $TaS(e)_2$, consisting of two 2H-like layers, separated by 1T-like layers [212, 213].

8.1.3 CHARGE DENSITY WAVES

Many TMDs, with their 2D-like nature, exhibit Charge Density Waves / Periodic Lattice Distortions behavior (CDW / PLD, the combined effects will be referred to as CDW in this work) at low temperatures, i.e. a new, larger periodicity spontaneously forms as the atomic positions over several unit cells and the associated electron density reorder to exchange electronic (band) energy with Coulomb energy of the atomic core positions. However, both the exact periodicity of the CDW with respect to the atomic lattice (some common in-plane periodicities being 3×3 and $\sqrt{13} \times \sqrt{13}$, although more complicated stripe-phases also occur) as well as the temperature dependence vary strongly between TMDs. In general, CDW behavior has a strong influence on the temperature-dependent properties of the material, making it interesting for applications. Furthermore, CDW, and its cousin spin density waves (SDW), are closely related to superconductivity in these materials, although it seems unclear if the CDW behavior competes with superconductivity or, alternatively, is a necessary component [214].

CDW behavior is the (two- or) three-dimensional equivalent of the Peierls transition, where dimerisation of a mono-atomic chain occurs at half-filling of the electron band [215]. The three-dimensional extension of the Peierls mechanism, Fermi surface nesting, suggests the need for large parallel parts of the Fermi surface to be connected by a CDW wave vector and therefore a strongly anisotropic Fermi surface, such as occurs in quasi-1D and -2D materials. In practice however, the Peierls mechanism is severely limited as a model. It suggests that in the 1D case, a CDW should always occur at low enough energy, but it was later realized the effect can already be suppressed in the presence of electron-electron interaction [216]. It turns out that more generally Fermi surface nesting has little to no predictive power for real materials, beyond materials with a strong 1D-like nature, i.e. atomic chains.

To properly model the CDW behavior in TMDs, Fermi surface nesting is therefore not sufficient. Instead, the combination of both the atomic cores and the electrons in the bands needs to be taken into account, including the electron-phonon coupling and its dependence on the relevant wave vectors [20, 217]. This does however significantly

increase the theoretical effort needed to understand the causes of CDW behavior. This is especially true in some materials, such as TaS_2, where the relative phase of the in-plane CDW in subsequent van der Waals layers is relevant [218–220].

8.1.4 TANTALUM DISULFIDE

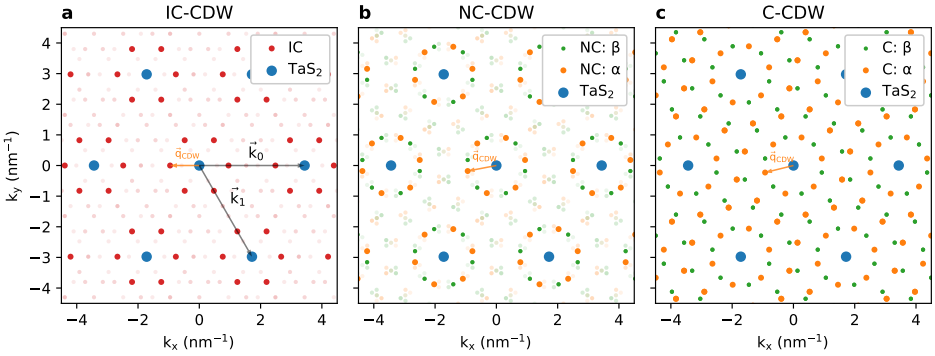

Figure 8.2: CDWs in 1T-TaS_2. *Schematic showing the different diffraction peaks for the different CDW phases occurring in TaS_2, incommensurate (IC), nearly commensurate (NC) and commensurate (C), with relevant parameters indicated. The atomic Bragg peaks of the TaS_2 are indicated in blue, the IC-CDW peaks in red. (See also Figure 1.1***c** *for a real space schematic of the CDW.) For the commensurate and nearly commensurate phase, the CDW peaks are indicted in orange and CDW peaks of the second possible orientation of the CDW (β-phase, vs α-phase) are indicated in green.*

The specific TMD studied here, TaS_2, exists in two bulk polytypes, 1T-TaS_2 and 2H-TaS_2. They have slightly different in-plane lattice constants, $a = 0.336$ nm and $a = 0.331$ nm respectively.[1] The former is meta-stable at room temperature, and can be acquired by quenching a crystal from high temperatures. Both polytypes exhibit CDW behavior. The 2H polytype only exhibits an (almost) commensurate 3×3 CDW below $T_c = 75$K in bulk [221], with the T_c rising up beyond 130K in the monolayer [222, 223]. However, the bulk 1T-TaS_2 polytype exhibits a more complicated set of CDW states. Starting from high temperatures, at $T \approx 540$K the crystal transitions into an incommensurate $\sqrt{13} \times \sqrt{13}$ CDW (IC-CDW) state, where the wave vectors of the CDW are parallel to the atomic lattice vectors (Figure 8.2**a**). At $T \approx 350$K, the material undergoes a transition to a nearly commensurate CDW state (NC-CDW, Figure 8.2**b**). In this state, the CDW vectors keep the same length as in the IC-CDW state, but rotate to $\theta_{NC} \approx 10.9°$. This is close to the commensurate angle of $\theta_C = \arccos\left(\frac{7}{2\sqrt{13}}\right) \approx 13.9°$, corresponding to a realspace CDW vector of $3\mathbf{a}_0 + \mathbf{a}_1$. However, in this state, it remains discommensurate with respect to the atomic lattice. This slight mismatch results in superdomains much larger than the $\sqrt{13} \times \sqrt{13}$ domains. At room temperature, the size of these NC-CDW superdomains can

[1] This slight difference in lattice constant can cause stacking domains just like in graphene on SiC as described in Chapter 7, see e.g. Ref. [17].

be expressed in terms of the mismatch between θ_{NC} and the commensurate angle θ_C:

$$L = \frac{a}{2\sin(\theta_C - \theta_{NC})} = \frac{0.336\text{nm}}{2\sin(13.9° - 10.9°)} \approx 7\,\text{nm} \tag{8.1}$$

This has been confirmed directly using STM [224], but also indirectly with X-ray diffraction [219]. The mismatch in k-space decreases (and therefore the real space period increases) for lower temperatures.

Below $T \approx 200$K the CDW undergoes a final transition and becomes commensurate (C-CDW) corresponding to a perfect match to the atomic lattice at $3\mathbf{a}_0 + 1\mathbf{a}_1$ and a rotation of the CDW vector of $\theta_C \approx 13.9°$ with respect to the atomic lattice vector (Figure 8.2**c**). In the atomic plane, this corresponds to 12 tantalum atoms in the unit cell moving towards the central final tantalum atom in a 'star-of-David' pattern.

The relative in-plane phase of the CDW in subsequent layers gives rise to an extra out-of-plane periodicity. While both the IC-CDW and the NC-CDW have a periodicity of 3 van der Waals layers along the c-axis (corresponding to face-centered cubic stacking of the CDW phases), literature states that the C-CDW either has a periodicity of 13 layers (iterating the center of the star-of-David over all 13 tantalum atoms in the in-plane unit cell) or is not periodic at all [218, 219].

The transition to C-CDW also incurs a transition to insulating behavior, just like in the simple Peierls model [213]. Finally, there are reports of stripe phases when warming the sample up from the C-CDW state [225] and "hidden" states accessed by laser excitation at low temperatures [226].

It is worth noting at this point that both the NC-CDW and C-CDW can exist in two equivalent mirror variants, referred to as α-phase and β-phase (green and orange in Figure 8.2). In a bulk 1T-TaS_2 sample, the whole sample exhibits a single orientation (which is then labeled α), but mixtures of both orientations can be induced by, for example, voltage pulses from an STM tip [227].

8.1.5 TOWARDS 2D

With the advent of TMDs as two-dimensional materials, CDWs in TMDs have received renewed interest. The CDWs extend out-of-plane in the TMDs. As the stacking of layers actually seems to play a role in stabilizing the CDW, let alone the fact that most CDW states have a periodicity of more than one van der Waals layer, the behavior of CDWs in the 2D limit has been an interesting open question. However, in addition to thickness, a number of other aspects seem to influence the CDW and the critical temperatures of its phase transitions, such as electrical or chemical doping, strain induced during exfoliation, increasing current densities in transport measurements, and even plain cracks in the sample and oxidation from ambient air. Unfortunately, all these factors become increasingly relevant when exfoliating a crystal to thinner layers.

These and other factors, as the following will show, complicate the study of how the CDW behavior changes for thinner samples closer to the true 2D limit using transport experiments or optical probes, as any change measured can be contributed either to (approaching) the 2D limit, or to one of these other extrinsic factors [228]. Here, we use Low-Energy Electron Microscopy (LEEM) to study local aspects of CDWs in TaS_2. Previous results using (Ultrafast) Low-Energy Electron Diffraction ((U)LEED) already showed that

low-energy electrons can be used to detect the presence of CDW, in particular in TaS_2 with CDWs above room temperature [218, 229]. Unlike these pure diffraction techniques LEEM can correlate the observation of CDWs with real space features using μLEED and dark field imaging modes, and thus help to distinguish the effect of (local) artifacts from intrinsic effects.

Beyond studying two-dimensional condensed matter physics, the second big potential of van der Waals materials is the possibility to combine different lattices and material properties by stacking layers. Arguably, the most famous example of this is superconductivity due to a flat band in 'magic' angle twisted bilayer graphene (See Chapter 6). Bottom-up combining 2D van der Waals layers does however suffer from the same complicating factors as described above. To study the layer interactions and the 2D limit of the CDW in TaS_2 and to try to avoid these issues, we will use an alternative approach here: by partially converting a single 1T crystal to 2H by annealing, we create a heterostack of 1T-like and 2H-like layers without the need to exfoliate single layers [230].

8.2 SAMPLE PREPARATION

Samples were prepared from exfoliated flakes. First, flakes were exfoliated using blue NITTO tape from a 1T-TaS_2 crystal purchased at `hq graphene`[2]. Next, these flakes were deposited directly onto silicon substrates with only a native oxide. To increase adhesion, the substrates were treated using an ozone cleaner[3] for approximately 20 minutes before flake deposition. This resulted in flakes of bulk-like thickness, i.e. in the order of 100 nm as measured by AFM (See Figure 8.3).

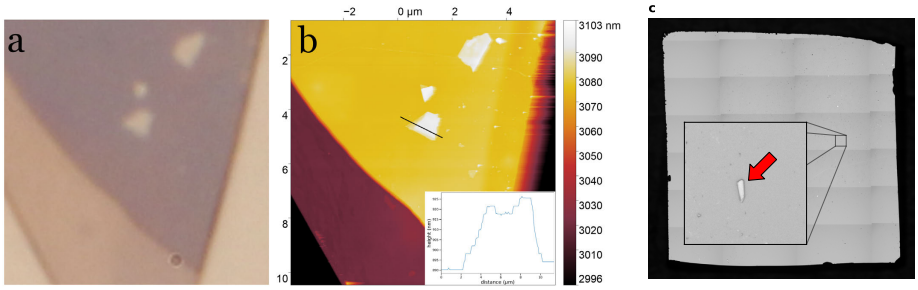

Figure 8.3: a, *Optical microscopy image of part of a TaS_2 flake.* ***b,*** *Corresponding AFM topography. Reproduced under CC-BY from [231].* ***c,*** *Optical overview of the full Si substrate. Red arrow indicates the flake in* ***a,b****. Full substrate is approximately* 5×5 *mm. Image taken by J.P. van Soest.*

Immediately after deposition from the tape onto the silicon, the substrates with flakes were mounted with a molybdenum backplate into the loadlock of the LEEM instrument and pumped down to a pressure lower than 1×10^{-6} mbar. This was achieved by exfoliating directly next to the instrument, to minimize exposure of exfoliated flakes to air, resulting in a time between deposition on the substrate and pump down of less than five minutes. For samples exposed to air for longer periods than this, no CDWs could be

[2] hq graphene, G. Meirstraat 1, 9728 TB Groningen, The Netherlands, `www.hqgraphene.com`
[3] Bioforce nanosciences UV/Ozone ProCleaner, nominal UV intensity of 19.39 mW/cm^2.

observed. After pump down, samples were transferred to the main UHV chamber (base pressure $< 1 \times 10^{-9}$ mbar) and annealed for at least an hour at a temperature of at least 200 °C (see below).

Annealing at a temperature of 200 °C is low enough to preserve the 1T polytype. A common technique in LEEM experiments to obtain a clean surface is to anneal beyond 450 °C in UHV to evaporate any surface adsorbates. Such annealing goes beyond the stability point of the 1T polytype and will convert parts of the sample to the 2H polytype.

8.3 PRISTINE 1T-TaS_2

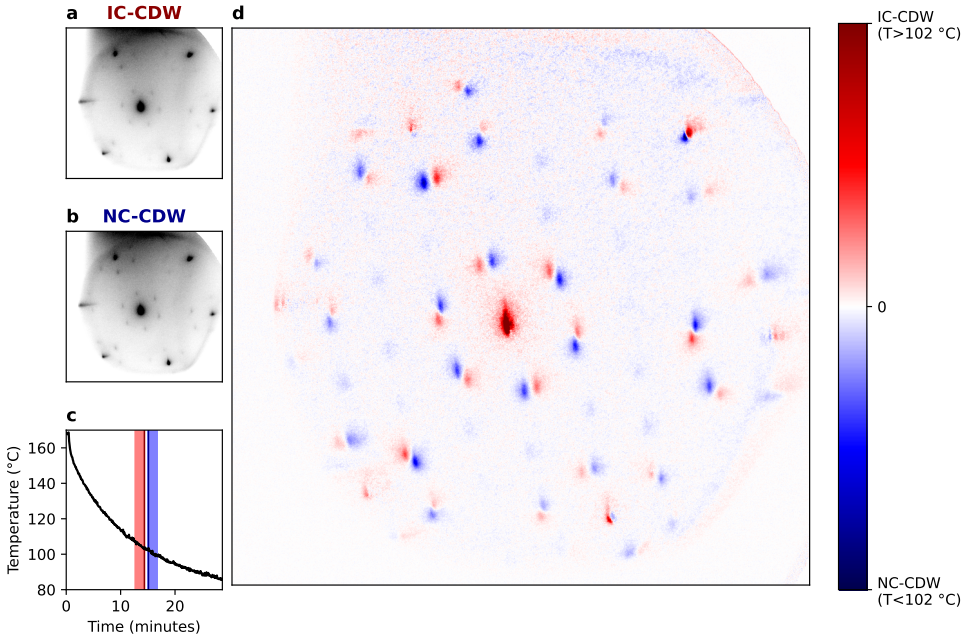

Figure 8.4: ***a,b,*** *Diffraction pattern for full beam illumination (~ 6μm across) of pristine 1T-TaS_2 respectively just above and just below the transition from incommensurate to nearly commensurate.* ***c,*** *Temperature during cooldown integration windows for* ***d*** *is indicated.* ***d,*** *Difference image of both diffraction patterns.*

For pristine 1T-TaS_2 samples prepared near-situ (as described above) and annealed at $T \approx 200$°C for several hours before cooling down again, weak CDW spots are visible. As expected for 1T-TaS_2, above $T \approx 102$°C (as measured using the IR-camera of the system)[4] an IC-CDW is present with the CDW vectors along the reciprocal atomic lattice vectors, and below $T \approx 102$°C a NC-CDW is present with the CDW vectors rotated away to almost a $\sqrt{13} \times \sqrt{13}$ grid, as shown in Figure 8.4. The measured IC–NC transition temperature is

[4] This is therefore an approximate value: all temperatures reported in this work are measured with an IR-camera without absolute calibration.

23K higher than values reported in literature, but this is well within the expected inaccuracy of the temperature measurement using the IR-camera.

However, we find surface quality to be far from optimal. This is evident by three aspects of the imaging: a high background intensity in the diffraction images obscuring the CDW spots, low contrast and smudging of features in real space images and finally contamination buildup during prolonged imaging at energies above ~ 5 eV.

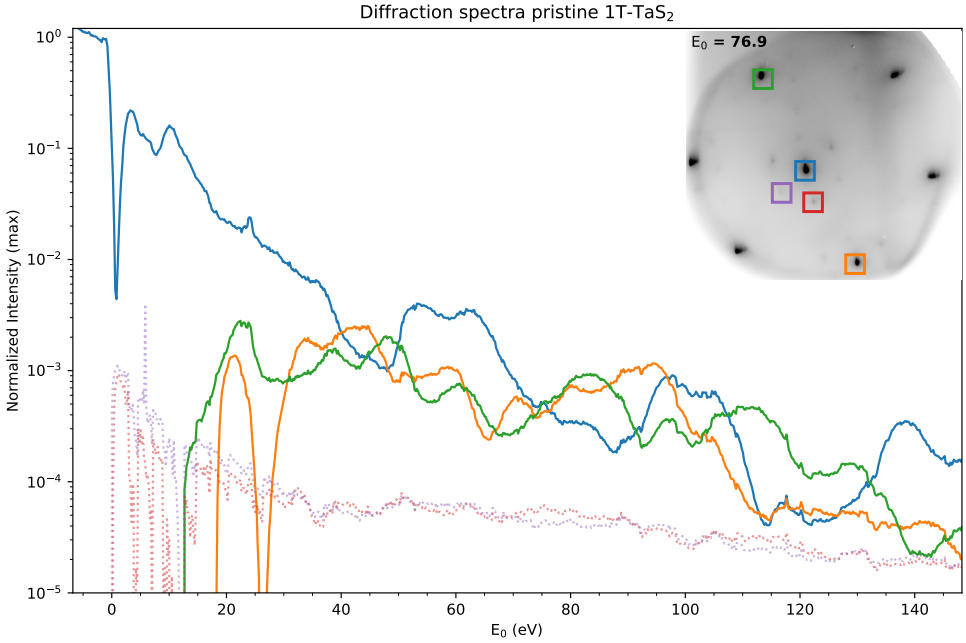

Figure 8.5: *LEED spectrum of pristine 1T-TaS_2 for the zeroth-order spot (blue) and two types of first-order diffraction spots (orange and green, as indicated in inset). The gain of the detector was actively tuned during the measurement as described in Section 3.3. Despite this, the NC-CDW spots (red and purple dashed) are very weak and hardly rise above the noise.*

Especially the contamination buildup is detrimental to any spectral imaging, with visible contamination buildup and signal deterioration during a single sweep of the landing energy. However, to serve as a reference for what is to follow, a LEED spectrum, where reflectivity for various diffraction spots is recorded as a function of landing energy E_0 [29], was measured on this surface in the NC-CDW state and is shown in Figure 8.5 [5]. In addition to the spectrum of the specular reflection, which corresponds to a bright field LEEM spectrum (as obtained for the mixed polytypes in the following), the spectra

[5] LEED-IV, LEED-I(V), LEED-IV spectrum, (for Low Energy Electron Diffraction Intensity vs Voltage) and their equivalent terms using LEEM and even LEER spectrum (Low Energy Electron Reflectivity spectrum) are used throughout literature to denote similar measurements. Here, LEED spectrum and LEEM spectrum are used to distinguish between diffraction and real space data, but the redundant 'IV' moniker is dropped, as measurements are properly normalized and therefore correspond to reflectivity as a function of landing energy and it can be easily confused with current-voltage transport measurements.

of two first order Bragg peaks are shown. Although the absolute intensity values at higher landing energies are lowered due to contamination, the relative positions of maxima and minima can still serve as a reference. A final note on these spectra: Just like in MoS_2 [31], neighboring first order peaks are inequivalent due to the 3-fold symmetry of the lattice. Similarly, although the spectra of the CDW-peaks barely rise above the background intensity, they also show signs of a 3-fold symmetry.

To reduce contamination buildup and contamination-induced beam damage, samples were annealed at temperatures beyond 450°C. Although this did reduce contamination buildup to workable levels, it has an additional effect of partially converting the 1T polytype to 2H, yielding a more complicated material system, as explained in the next section.

8.4 MIXED POLYTYPES

Before considering the results on mixed polytype samples, we consider the complexity of mixed polytypes. Due to the limited penetration depth of electrons at LEEM energies, in general the top layer contributes most to the reflectivity spectrum, with each subsequent layer contributing exponentially less. Therefore, we start out considering only two layers of TaS_2. For a bilayer of TaS_2, with each layer either 1T-like or 2H-like, several inequivalent stackings exist, even when taking into account rotation, mirror symmetry and relative in-plane position, as relevant for bright field LEEM (and without taking into account CDWs).

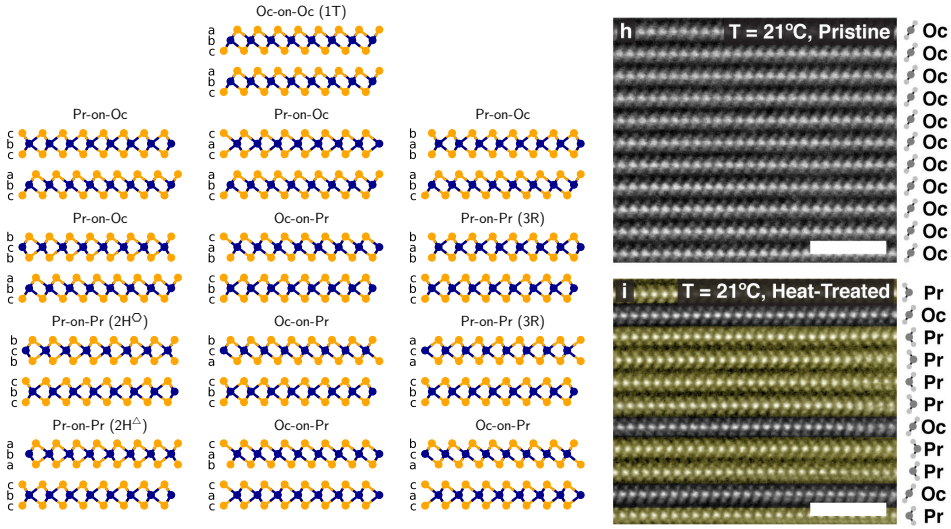

Figure 8.6: (left) *Schematic of possible stackings of two layers of TaS_2 either of the Oc or Pr type. Labels (abc) indicate the sublattice positions of the atoms in the layer.* ***(right)****: Stacking of pristine and (heat-treated) mixed state TaS_2 as measured by HR-TEM, scalebars are 2 nm. Reproduced under CC-BY from Ref. [230].*

Due to the three atomic layers in the unit cell, stacking these two layers has the same

complexity as stacking six graphene layers: subsequent layers can not occupy the same sublattice, leaving two out of three sublattices as a possibility for each added layer (in graphene, equivalently, the subsequent empty sublattices can not occupy the same position to obtain a Bernal stacking). Therefore, before taking symmetries into account, there are $2^5 = 32$ possible stackings.

However, taking into account the symmetries and the fact that all layers are formed from a pristine 1T crystal, only thirteen possible stackings remain[6], as all 1T layers must have the same orientation and sublattice (as corroborated by High resolution transmission electron microscopy (HR-TEM) data, see Figure 8.6):

- Oc-on-Oc: 1 option (bulk-like 1T)
- Oc-on-Pr: 4 options (2 for the top sulfur of the Pr layer times 2 for the Ta).
- Pr-on-Oc: 4 options (similarly).
- Pr-on-Pr: 4 options (2× 3R-like stacking (Ta on top of S or S on top of Ta), $2H^{\hexagon}$, and $2H^{\triangle}$).

Notably, using HR-TEM in Ref. [230] no 3R-like stacking was observed and all subsequent 2H-like layers were $2H^{\hexagon}$, as opposed to the supposedly $2H^{\triangle}$ in bulk.

As suggested by this number of different possibilities to stack only two layers, a wide variety of LEEM spectra could be expected if annealing results in a state of mixed polytypes.

However, if energy differences between different stackings are too large, some of these stacking options might still not occur. To compare, the authors of Ref. [17] report on STM observations of two Oc-on-Pr stackings, with the other two options not occurring, because the low temperature laser-induced polytype transformation they apply only influences the top-most sulfur layer. The fact that the parallel domain boundaries in their results are twinned, i.e. move closely together in pairs, does indicate an energy difference between the observed stackings, but at the same time show that the energy difference is small enough for both stackings to co-exist.

8.4.1 SPECTRA

Indeed, after annealing at 450°C, a cleaner surface is achieved than when annealed at lower temperatures[7], as indicated by higher contrast LEEM images and a higher intensity of the Bragg peaks compared to secondary electrons.

For almost all samples, a complex set of areas with different reflectivity appears, even after annealing overnight, suggesting indeed a state of mixed polytypes, as previously reported in TEM work [230].

[6] From (unpublished) twisted MoS_2 data, it is known that relative lattice positions are relevant to the BF LEEM spectra, as contrast is observed in ~ 0° (3R-like) stacked layers and the spectra both show differences compared to 2H-like stacking.

[7] There is one alternative explanation for the observed behavior that could be considered. By the nature of the exfoliation process, there are two types of flake surface: a surface that was in contact with the tape, and surface that was cleaved of the crystal upon transfer to the substrate, which never touched the tape. *If* a crystal still contains trace amounts of different polytypes, the internal lattice mismatch would cause it to preferentially tear in this area, especially on the last transfer, causing clean, but mixed polytype surfaces.

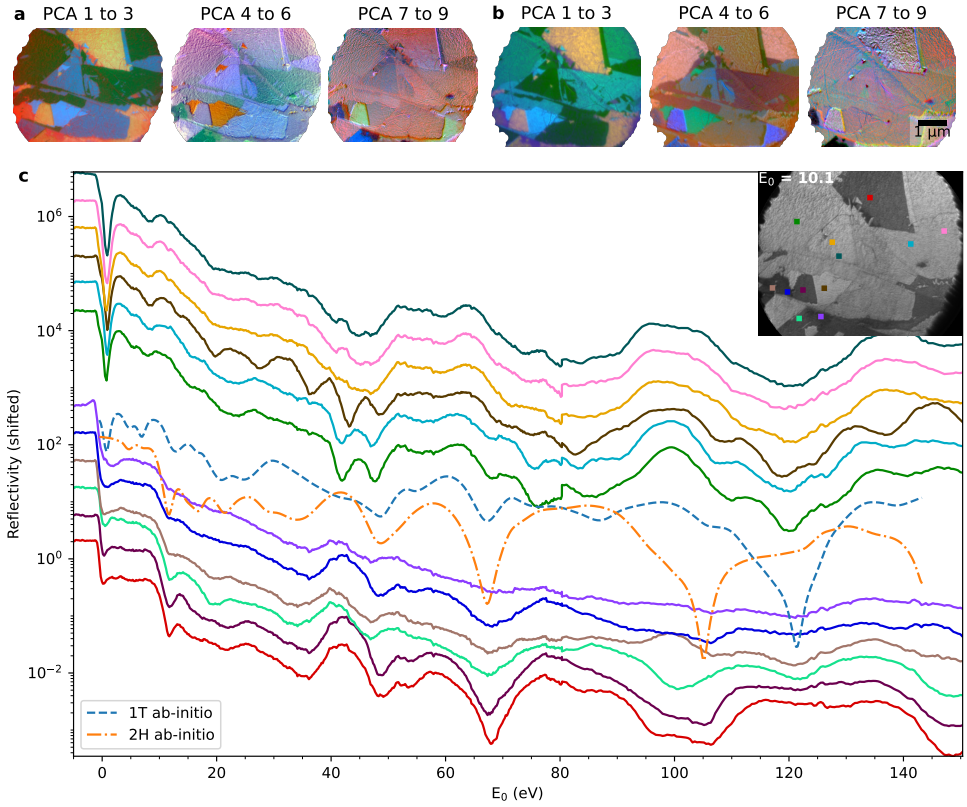

Figure 8.7: a, *PCA decomposition visualizations of BF-LEEM spectra for 0–80 eV [35]* ***b,*** *Same, but starting at 80eV up to 150 eV.* ***c,*** *LEEM spectra of different mixed polytypes. Curves are offset for clarity, with spectra resembling 1T at the top and those more similar to 2H below. The yellow curve (third from top) most closely resembles the pristine 1T curve in Figure 8.5. A slight mismatch at 80 eV is due to the changes between taking the two parts of these IV curves. (Separate datasets at same location). For comparison, ab-initio calculations of 1T-TaS_2 and 2H-TaS_2, both without any CDW taken into account, are shown as dashed and dashed-dotted respectively.*

Recording reflectivity as a function of E_0 using real space bright field (i.e. using the specular reflection), we observe at least twelve different area types, as shown in Figure 8.7**a,b**, visualized using the PCA decomposition described in Chapter 3. Some differences in the spectra themselves (Figure 8.7**c**) are very subtle, corresponding to a small shift in the energy direction, but other spectra show larger deviations.

The observed spectra split into two categories: about half of the curves are similar to the curve of pristine, low temperature annealed 1T-TaS_2 in Figure 8.5, with a steep minimum directly at 0 eV, minima around 80 and 120 eV and a maximum around 100 eV. These spectra are shown at the top of Figure 8.7**c**. The other set of curves has opposite traits, with only a very shallow minimum around 0 eV and large plateaus of high intensity around 80 and 120 eV. These are shown at the bottom of Figure 8.7**c**. Unfortu-

nately, comparison of these spectra to theory using standard calculations is complicated by the presence of CDW and the single experimental curve available per area type in bright field LEEM experiments. Ab-initio calculations (as described in Refs. [116–118]) of the bulk 1T and 2H polytypes are shown dashed and dashed-dotted in Figure 8.7**c**. A rudimentary tensorLEED approach similarly not taking into account the CDW, but simulating different stackings of Pr and Oc layers has further confirmed this and additionally suggests that the other observed differences could indeed be attributed to different stackings (See Figure D.3 in Appendix D) [232]. However, for a specific assignment of the different LEEM spectra to specific stackings, ab-initio calculations of different stackings are needed and in addition spectra of 1T-like areas above the IC-CDW onset are needed to assess the influence of the CDW on the BF-LEEM spectra.

8.5 CHARGE DENSITY WAVE STATES

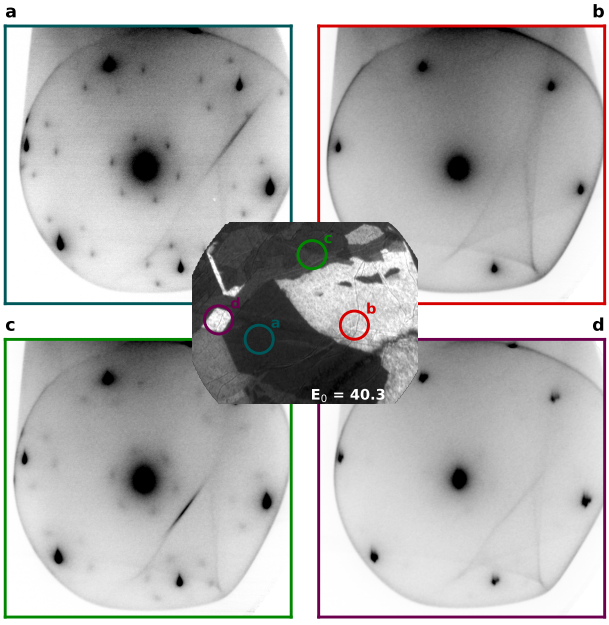

Figure 8.8: *μLEED patterns of different areas at elevated temperatures. Frame colors correspond to spectra of similar areas in Figure 8.7. The 1T-like areas (**a,c**) show ICCDW spots, the 2H-like area (**b**) does not show any CDW spots. Very low intensity IC-CDW spots are visible in 2H-like (**d**), which could be due to a CDW in a lower layer. However, it can not be excluded that these are from edges around the 2H-like area, but within the aperture. Color assignment of (c) is not 100% certain, a mix of areas might be present there as it lies outside of the area imaged in Figure 8.7. All diffraction patterns were taken at $E_0 = 56$ eV, $T \approx 233°C$.*

Upon cooling down well below the IC-CDW threshold, the assignment into two classes of 1T-like and 2H-like areas is further corroborated by the μLEED measurements in Figure 8.8: taking diffraction patterns of single areas, 1T-like areas have (varying degrees of) IC-CDW order, which is absent in 2H-like areas, as expected for the respective bulk polytypes.

A difference compared to measurements on pristine 1T samples is that upon cooling down further to below $T \approx 125°C$, a twin rotational order CDW appears, i.e. both the α and β phase coexisting, as shown in Figure 8.9**a**. Notably, this transition temperature is

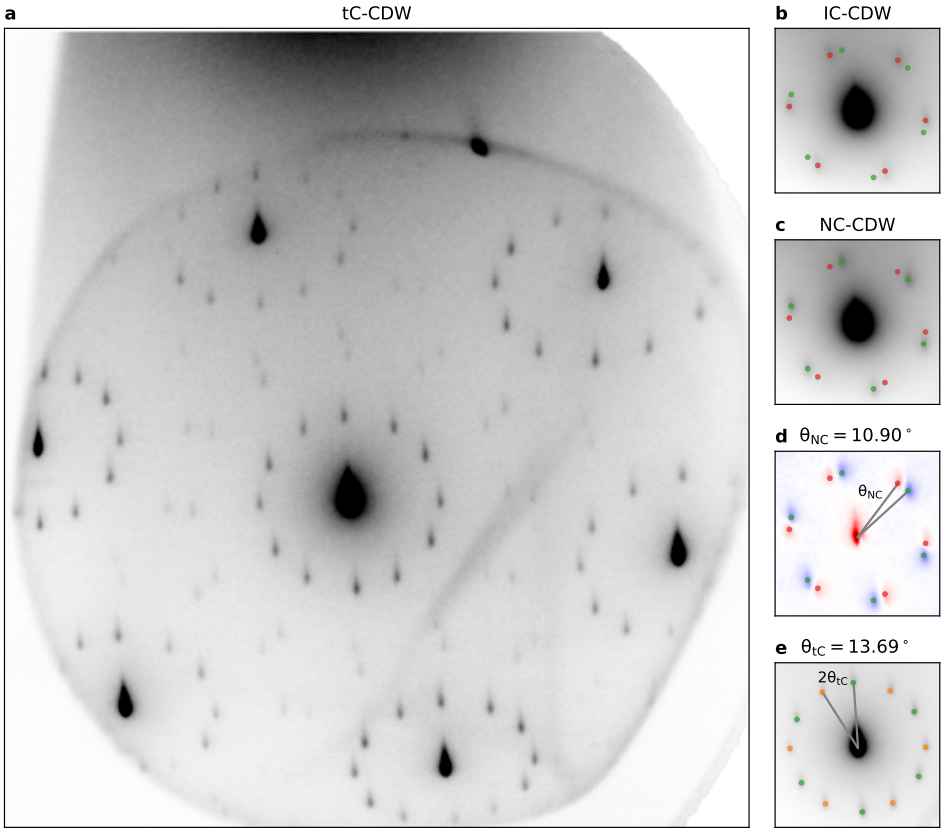

Figure 8.9: ***a,*** *Diffraction pattern of an annealed sample at 56 eV, taken after cooling, with an illumination aperture of 2 µm effective diameter. A twin pattern of CDW peaks is visible, i.e. including both α and β phase peaks.* ***b,c,*** *Detected diffraction peaks in the pristine sample. Same data as Figure 8.5.* ***d,*** *Difference image of* ***b,c*** *with the detected twist angle θ_{NC} between the NC phase and the IC phase (which is parallel to the atomic lattice). The reported angles are the average of all six angles to cancel out experimental distortions of the diffraction plane.* ***e,*** *Crop of* ***a*** *with the detected diffraction peaks and the twist angle θ_{tC} with respect to the atomic lattice.*

about 23°C higher than for the pristine IC–NC transition.[8] What is more, when heating again, the IC-CDW spots only start appearing at $T \approx 136$°C, and the diffraction spots corresponding to twinned phases remain all the way up to $T \approx 168$°C, indicating a relatively large hysteresis and coexistence of all three phases in the illuminated area.

In the twin rotational CDW order, the angle between the CDW vector and the atomic lattice is measured to be $\theta_{CDW} = 13.7°$ (Figure 8.9**e**), while for the pristine NC-CDW we measure $\theta_{NC} = 10.9°$ (Figure 8.9**d**). Furthermore, the second order CDW bragg peaks

[8] This *difference* between temperatures is significant as these were measured on the same instrument. Although the *accuracy* of the measurements using the IR-camera is relatively low, the measurements should be *precise* to within 5 K.

are as sharp as the first order peaks, i.e. no broadening due to splitting is observed (cf. Figure 8.4). As the observed CDW angle is much closer to commensurate than observed for the nearly-commensurate state and splitting is expected for the NC-CDW state, we conclude that the measured state is actually a twinned *commensurate* CDW (tC-CDW), even though the expected (and observed) CDW around room temperature in pristine 1T-TaS_2 is *nearly commensurate*.

This twinned rotational pattern has been observed before in the early days of TEM measurements [213, 233]. At the time, it was also concluded that the pattern actually corresponds to tC-CDW (as opposed to a NC variant). The pattern was attributed to a $4H_b$ polytype, with alternating layers of Oc and Pr layers of alternating rotation, as no in-plane spatial domains for these CDW orders were observed. This polytype would allow separate Oc layers on top of each other to exhibit opposing orientations, with adjacent Pr layers providing a sufficiently different environment to allow for the CDW state to be commensurate and the projection along the c-axis of the TEM measurement causing the superposition of both sets of peaks. However, as will become clear in the following, our observations do not match this attribution.

8.5.1 IN-PLANE CDW DOMAINS

In the previous section we described μLEED measurements, which already use the unique capability of a LEEM to do local LEED measurements of areas imaged. A further obvious capability of LEEM to apply to charge density wave order is Dark Field imaging to directly observe the spatial distribution of the CDWs.

Contrary to earlier TEM measurements on the twin rotational state, we *do* observe in-plane rotational domains when imaging using the tC-CDW diffraction spots, as shown in Figure 8.10. Comparing different dark field images, 1T-like areas exhibit two complementary sets of bright domains, as shown by composite images in Figure 8.10, with one corresponding to the α phase, and the other to the β phase, i.e. rotated in the opposite direction with respect to the atomic lattice directions. These domains were observed in multiple samples prepared in the way described (and confirmed semi-independently at the TU Chemnitz by P. Schädlich, see Figure D.5).

Although all 2H-like areas appear white in these images, no diffraction spots corresponding to CDWs were observed in any 2H-like area, just like in Figure 8.8**b**. However, 2H-like areas exhibited a much higher background intensity in diffraction at the imaging energy used, indicating a higher inelastic electron reflectivity of the 2H-like areas than in the 1T-like areas. (A fit of the diffraction peak profiles can be found in Appendix D, Figure D.6.) Furthermore, close inspection of the composite DF images in Figure 8.10 reveals that the domains in 1T-like areas occur in two different intensities (a boundary between a bright and dark area is indicated with a dark red line in Figure 8.7**b**). From the overlap of these DF images with the area used for spectral imaging in Figure 8.7, we conclude that the area corresponding to the dark green curve in Figure 8.7 (sixth from top) exhibits a dimmer CDW than the area corresponding to the ochre one (third from the top; this spectrum is closest to the pristine 1T spectrum). As both of these spectra are 1T-like, they are both assumed to have an Oc top layer. This indicates an influence of the layer below on the observed magnitude of the CDW. The increased contrast even suggests that no vertical mixing of the orientation domains occurs, i.e. that α-phase do-

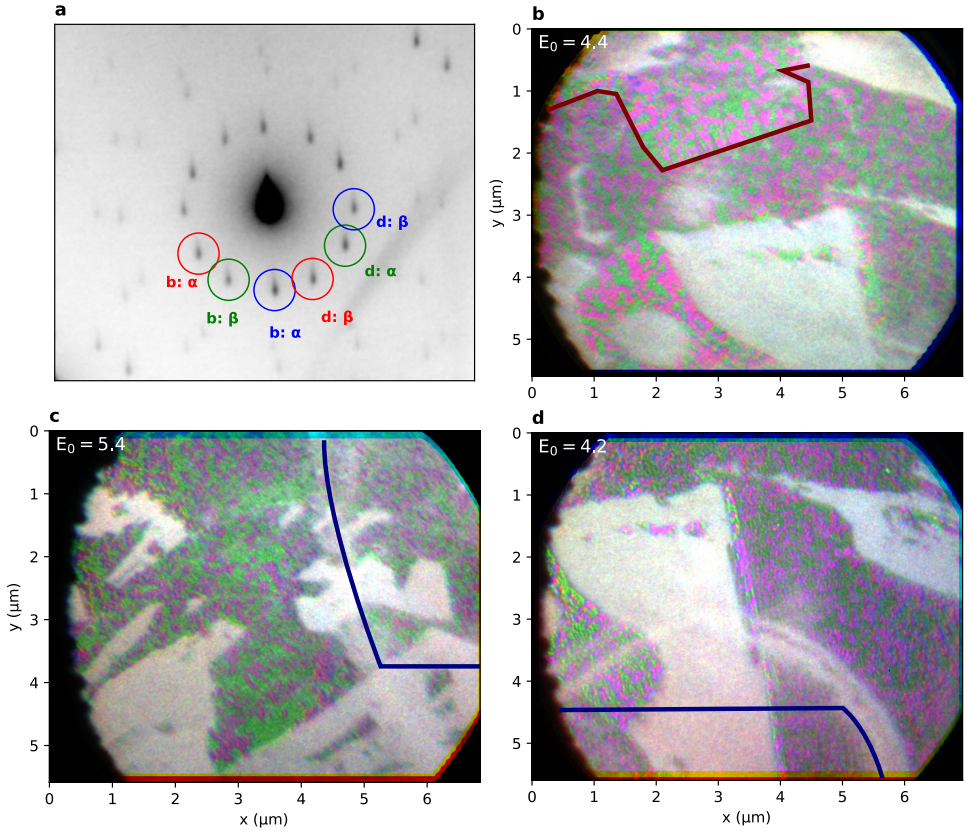

Figure 8.10: ***a,*** *Zoom of the tC-CDW diffraction pattern shown in Figure 8.9* ***a*** *indicating the aperture positions used for Dark Field LEEM.* ***b-d,*** *Composite Dark Field of CDW domains, using spots indicated in* ***a*** *of slightly different areas (c uses different but equivalent spots as d). By using three spots, of which two equivalent, the one orientation appears green, while the other appears purple, as both the red and the blue channel contribute there. Large areas of white correspond to 2H-like areas. Circular spots of white in* ***b*** *correspond to contamination due to µLEED measurements in Figure 8.8. In dark red the edge of a bright CDW domain is indicated (see main text). Half rings in* ***c,d*** *correspond to contamination at the edge of the beam during the measurement of the spectra in Figure 8.7: the boundary of the field-of-view of that measurement is indicated with dark blue lines.*

mains in the ochre areas do not lie on top of β domains in the layer below, or vice versa. Although a relative phase shift of the CDW in the underlying layer with respect to the CDW in the top layer could cause bright field and dark field contrast, the strict equivalency of the brightness of the different dark fields and the fact that the orientational (α versus β phase) domains are much smaller than these areas indicates that these differences are caused by the polytype of the underlying layer.

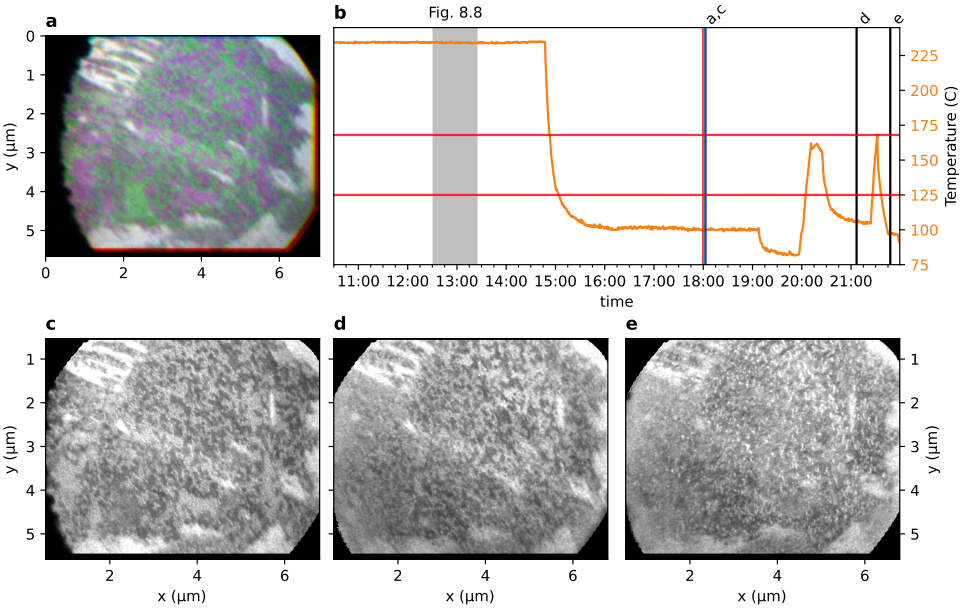

Figure 8.11: a, *Composite Dark Field image with twin rotational domains in green and purple.* ***b,*** *Temperature during temperature cycling experiment. Vertical lines indicate times of subsequent images, the time span during which the data in Figure 8.8 was taken is shaded gray.* ***c-e,*** *Dark Field LEEM images of the same area after heat cycling to IC-CDW. The domains reappear in a similar fashion, but orientation (α or β) are uncorrelated to earlier cycles.*

A question in the case of any observation of domains in a complicated system like this would be whether the observed domains are not simply a result of pinning to extrinsic defects, which could have been generated by the annealing or during exfoliation. To check this, the sample was thermally cycled into the IC-CDW state and back. As shown in Figure 8.11, similar domains reform after thermal cycling, but the shapes (i.e. what position on the sample is α or β-phase) is uncorrelated to the previous cycle, indicating the domains are no direct consequence of sample geometry or local strain.

8.6 DISCUSSION

To consider the implications of the observed tC-CDW state with in-plane domains and what it means for the NC-CDW state in pristine 1T-TaS_2, we first need to reconsider the role of the ~ 7 nm diameter superdomains in the NC-CDW caused by the near-commensurability. Although the presence of these superdomains at room temperature and the apparent suppression of the CDW amplitude at the domain boundaries in STM (See e.g. Ref. [225, 234]) are sometimes seen as an indication of a low spatial coherence, they are in fact the opposite, as the phase of the CDW shifts consistently over the length scale of multiple domains. Therefore, a high spatial coherence is needed for the NC-CDW to be energetically favorable over the C-CDW. Furthermore, the fact that meso-

scopic/macroscopic pristine bulk samples exhibit only a single orientation of the CDW (i.e. only α-phase, both at room temperature / NC-CDW as well as low temperature C-CDW) also indicates very high spatial coherence.

The hexagonal superdomains are similar to the stacking domains in twisted bilayer graphene in more than one way. Although globally the NC-CDW lattice vector is rotated away from the C-CDW lattice vector, within a domain it is actually equal to the C-CDW vector [234, 235], with all the phase shift concentrated in the domain boundaries, just like the graphene lattices are commensurate within the TBG stacking domains, but the relative (lattice-) phase shifting in the shear domain boundaries to maintain a globally consistent lattice displacement corresponding to the twist.

Second, just like in TBG for incommensurate twist angles, the hexagonal superdomains in the NC-CDW phase are irregular, with each domain slightly different than its neighbors, but this is a result of the incommensurability of the NC-CDW vectors, not to be confused with disorder, as the latter would actually cause smeared CDW diffraction spots, which are not observed in electron diffraction and X-ray diffraction [219, 228, 229].

In the mixed polytype state after annealing, however, we observe twinned commensurate CDW domains with a characteristic size of ~ 150 nm. (Details about the domain size extraction are given in Appendix D, see Figure D.4.) This means the spatial coherence of the CDW is limited by the domain boundaries between α and β domains, even though the domain size is still an order of magnitude larger than the NC-CDW superdomains in bulk 1T-TaS_2. Apparently so much so, that the NC-CDW state is no longer energetically favorable.

An alternative assumption would be that the measured value of $\theta_{tC} \approx 13.7°$ does not correspond to a commensurate angle, but to a very nearly commensurate state. In that case, by Equation 8.1, the NC-CDW superdomains would have a corresponding size $L \approx 49$ nm, much closer to the observed characteristic size of the orientation domains. In this case interaction between the CDW and the rotational domains seems inevitable.

A further question is whether the observed tC-CDW state with domains is an inherent property of specific mixed polytype stackings or is due to some other property like lattice strain or contamination. Although the influence of such extrinsic properties cannot be fully excluded, the fact that the tC-CDW state reproduces in different local orientations after thermal cycling and the fact that the same state was reproduced on other samples and with slight variations of the annealing procedure point to an inherent property.

TEM measurements on comparable tC-CDW states [230, 233], however, reported no distinguishable domains. Although at first sight those observations seem incompatible with the reported domains here, it should be noted that while LEEM measurements are inherently surface sensitive, meaning for any LEEM signal the top-layer dominates the result, TEM projects through the entire sample. It therefore seems plausible that the lack of observation of CDW domains in these TEM measurements could be caused by the averaging along the c-axis of the CDW of different orientations in various 1T-like layers isolated from each other by Pr layers.

A final question is whether the tC-CDW angle compared to the nearly-commensurate angle in pristine 1T-TaS_2 is really due to the limited size of the domains, or an inherent property of the polytype stackings.

As shown in Figure 8.12, larger domains were observed on another sample, which

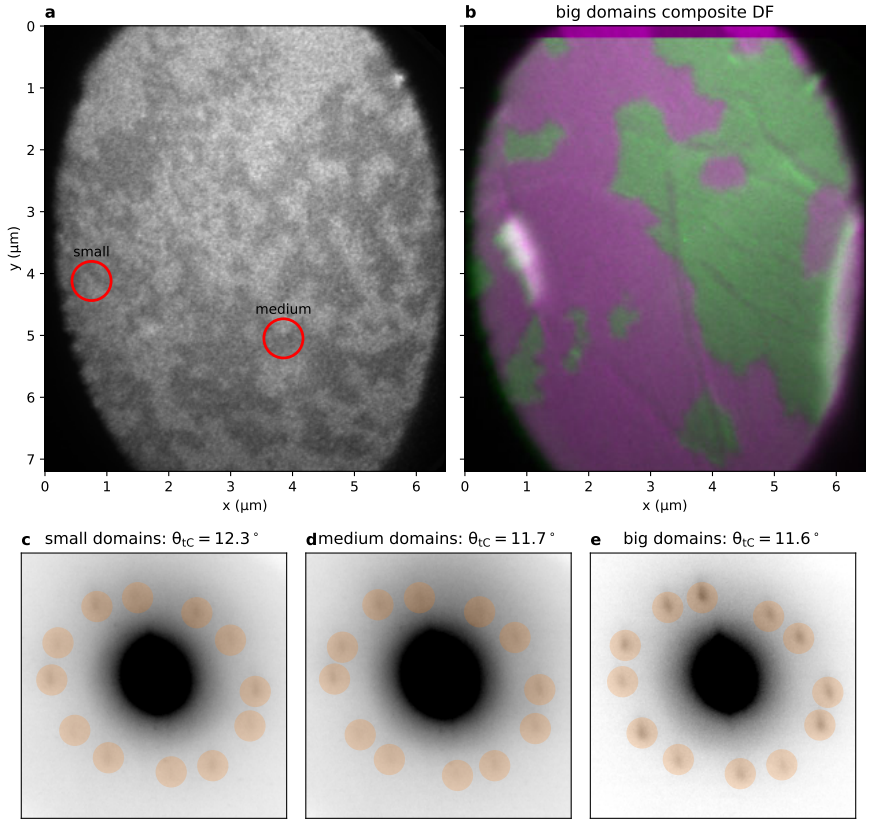

Figure 8.12: ***a,*** *Dark Field LEEM measurement on a newly annealed sample, showing various domain sizes. µLEED apertures of* ***c,d*** *are indicated with red circles. The 'small' domain areas still corresponds to somewhat larger domains than observed in the other sample.* ***b,*** *Composite dark field LEEM image of a different location on the same flake showing very large, micron-sized domains.* ***c,d,*** *Zoomed µLEED patterns with tC-CDW peaks marked, corresponding to* $\theta_{tC} \approx 12.3°$ *and* $\theta_{tC} \approx 11.7°$ *respectively.* ***e,*** *LEED pattern of the entire gun spot of the area shown in* ***b****, with* $\theta_{tC} \approx 11.6°$*. All measurements in this figure taken at* $T \approx 70°C$*.*

was annealed for a much shorter time. However, due to unrelated reasons, imaging conditions on that sample were unfortunately not good enough to obtain spectroscopic measurements or even detailed diffraction patterns to measure θ_{CDW} accurately. Nevertheless, cooling rates through the transition were similar to other cooldowns at $\sim 0.05\,\mathrm{K/s}$ as this is limited by the thermal mass and dissipation of the sample stage.

However, the limited evidence gathered from this sample does *suggest* that θ_{tC} decreases towards the 1T bulk value of $\theta_{\mathrm{NC}} = 10.9°$ for larger domains, as shown in Figure 8.12**c-e**, but strong distortion and low diffraction intensity causes a large uncertainty on these measurements (although independent reproduction of θ_{tC} for small domains, see Figure D.5 in Appendix D, seems to indicate the error is small enough for the mea-

sured difference to be significant).

8.6.1 COMPARISON TO LOW-TEMPERATURE HIDDEN STATE

A different, as-of-yet undiscussed CDW state in 1T-TaS_2 is the metallic, so-called 'hidden' (H) phase, which can be accessed at low temperatures by exposing the sample to a laser pulse or electrical excitation [227, 236, 237]. This state exhibits a irregular mosaic of shifted commensurate domains, where the changed relative stacking order of the CDW in subsequent layers seems responsible for the transition from an insulating to a metallic state [236]. This H-phase exhibits a diffraction pattern with an angle relative to the atomic lattice that is closer to the C-CDW than the NC-CDW phase, similar to the tC-CDW reported here [226, 238]. However, contrary to the tC-CDW state, the domains (almost) all remain in the α-phase in the H-phase and the H-phase reverts to the C-CDW phase upon heating before converting to the NC-CDW phase.

8.7 CONCLUSION

We have studied charge density wave states in TaS_2 using LEEM. In particular, we have studied mixed polytype states which occur after annealing a 1T-TaS_2 sample above its stability threshold of $T \approx 550$K. We have shown that a wide variety of different areas can be distinguished on such samples using spectroscopic LEEM. By comparing to ab-initio calculations, we distinguish areas with a 1T-like top layer which *do* host charge density wave states and areas with a 2H-like top layer which *do not* show any sign of charge density wave states in LEEM at room temperature and above. Many more differences in the spectra are observed, which can be due to difference in polytype order, differences in relative stacking of these layers or even different CDW states.

Interestingly, the CDW states in these mixed polytype samples show significant differences compared to the behavior in bulk 1T-TaS_2. Where in the bulk 1T material a single α-phase orientation occurs, here both possible orientations occur in a twinned orientation CDW. Using dark field LEEM, we show that the twinned orientation is due to rotational domains with a characteristic size of ~ 150 nm.

Furthermore, we have shown that the twinned CDW in these small domains is actually commensurate (tC-CDW) instead of the nearly commensurate CDW observed in the 1T bulk, and we found significantly higher transition temperatures than in bulk 1T and a large hysteresis to the IC-CDW state.

Finally, we have shown that the domain size is not always so small, and we observed indications that the domain size itself might cause the shift from NC to C, due to a lack of spatial coherence needed to realize an energy benefit for the NC state.

However, to fully confirm this influence and its potential implications for the nature of the tC-CDW in these samples and even of the NC-CDW in the pristine 1T-TaS_2 itself, two things are needed: first, confirmation of the precise stacking configurations in these samples, for example by comparing to theoretical calculations of the LEEM spectra of different stackings. Second, connecting this to more precise measurements on the relation between domain size and θ_{tC}. This way, it would be possible to infer whether the observed tC-CDW state is inherent to the 2D-limit of 1T-TaS_2, or due to some other mechanism.

REFERENCES

17. J. Ravnik, I. Vaskivskyi, Y. Gerasimenko, et al. Strain-Induced Metastable Topological Networks in Laser-Fabricated TaS_2 Polytype Heterostructures for Nanoscale Devices. *ACS Applied Nano Materials* **2,** 3743–3751. doi:10.1021/acsanm.9b00644 (2019).

20. J. Henke, F. Flicker, J. Laverock & J. van Wezel. Charge order from structured coupling in VSe_2. *SciPost Physics* **9,** 056. doi:10.21468/SciPostPhys.9.4.056 (2020).

29. J. I. Flege & E. E. Krasovskii. Intensity-voltage low-energy electron microscopy for functional materials characterization. *Physica Status Solidi - Rapid Research Letters* **8,** 463–477. doi:10.1002/pssr.201409102 (2014).

31. T. A. de Jong, J. Jobst, H. Yoo, et al. Measuring the Local Twist Angle and Layer Arrangement in Van der Waals Heterostructures. *physica status solidi (b)* **255,** 1800191. doi:10.1002/pssb.201800191 (2018).

35. T. A. de Jong, D. N. L. Kok, A. J. H. van der Torren, et al. Quantitative analysis of spectroscopic low energy electron microscopy data: High-dynamic range imaging, drift correction and cluster analysis. *Ultramicroscopy* **213,** 112913. doi:10.1016/j.ultramic.2019.112913 (2020).

116. E. E. Krasovskii, F. Starrost & W. Schattke. Augmented Fourier components method for constructing the crystal potential in self-consistent band-structure calculations. *Physical Review B* **59,** 10504–10511. doi:10.1103/PhysRevB.59.10504 (1999).

117. E. E. Krasovskii. Augmented-plane-wave approach to scattering of Bloch electrons by an interface. *Physical Review B* **70,** 245322. doi:10.1103/PhysRevB.70.245322 (2004).

118. V. U. Nazarov, E. E. Krasovskii & V. M. Silkin. Scattering resonances in two-dimensional crystals with application to graphene. *Phys. Rev. B* **87,** 041405. doi:10.1103/PhysRevB.87.041405 (4 2013).

211. D. Lin, S. Li, J. Wen, et al. Patterns and driving forces of dimension-al-i-ty-de-pendent charge density waves in 2H-type transition metal dichalcogenides. *Nature Communications* **11,** 2406. doi:10.1038/s41467-020-15715-w (2020).

212. J. Wilson & A. Yoffe. The transition metal dichalcogenides discussion and interpretation of the observed optical, electrical and structural properties. *Advances in Physics* **18,** 193–335. doi:10.1080/00018736900101307 (1969).

213. J. A. Wilson, F. J. Di Salvo & S. Mahajan. Charge-density waves and superlattices in the metallic layered transition metal dichalcogenides. *Advances in Physics* **50,** 1171–1248. doi:10.1080/00018730110102718 (2001).

214. A. H. Castro Neto. Charge Density Wave, Superconductivity, and Anomalous Metallic Behavior in 2D Transition Metal Dichalcogenides. *Physical Review Letters* **86,** 4382–4385. doi:10.1103/PhysRevLett.86.4382 (2001).

215. K. Rossnagel. On the origin of charge-density waves in select layered transition-metal dichalcogenides. *Journal of Physics: Condensed Matter* **23,** 213001. doi:10.1088/0953-8984/23/21/213001 (2011).

216. P. B. Littlewood & V. Heine. The effect of electron-electron interactions on the Peierls transition in metals with strong nesting of Fermi surfaces. *Journal of Physics C: Solid State Physics* **14,** 2943–2949. doi:10.1088/0022-3719/14/21/012 (1981).

217. M. D. Johannes & I. I. Mazin. Fermi surface nesting and the origin of Charge Density Waves in metals. *Physical Review B* **77,** 165135. doi:10.1103/PhysRevB.77.165135 (2008).

218. G. von Witte, T. Kißlinger, J. G. Horstmann, et al. Surface structure and stacking of the commensurate $(\sqrt{13}\times\sqrt{13})R13.9^\circ$ charge density wave phase of 1T–TaS_2(0001). *Physical Review B* **100,** 155407. doi:10.1103/PhysRevB.100.155407 (2019).

219. A. Spijkerman, J. L. de Boer, A. Meetsma, G. A. Wiegers & S. van Smaalen. X-ray crystal-structure refinement of the nearly commensurate phase of 1 T–TaS_2 in (3 + 2)-dimensional superspace. *Physical Review B* **56,** 13757–13767. doi:10.1103/PhysRevB.56.13757 (1997).

220. S.-H. Lee, J. S. Goh & D. Cho. Origin of the Insulating Phase and First-Order Metal-Insulator Transition in 1T-TaS_2. *Physical Review Letters* **122,** 106404. doi:10.1103/PhysRevLett.122.106404 (2019).

221. G. A. Scholz, O. Singh, R. F. Frindt & A. E. Curzon. Charge density wave commensurability in 2H-TaS_2 and Ag_xTaS_2. *Solid State Communications* **44,** 1455–1459. doi:10.1016/0038-1098(82)90030-8 (1982).

222. M. Lee, M. Šiškins, S. Mañas-Valero, et al. Study of charge density waves in suspended 2H-TaS_2 and 2H-$TaSe_2$ by nanomechanical resonance. *Applied Physics Letters* **118,** 193105. doi:10.1063/5.0051112 (2021).

223. D. Zhang, Y. Wu, Y.-H. Su, et al. Charge density waves and degenerate modes in exfoliated monolayer 2H-TaS_2. *IUCrJ* **7,** 913–919. doi:10.1107/S2052252520011021 (2020).

224. X. L. Wu & C. M. Lieber. Direct observation of growth and melting of the hexagonal-domain charge-density-wave phase in 1T-TaS_2 by scanning tunneling microscopy. *Physical Review Letters* **64,** 1150–1153. doi:10.1103/PhysRevLett.64.1150 (1990).

225. R. E. Thomson, B. Burk, A. Zettl & J. Clarke. Scanning tunneling microscopy of the charge-density-wave structure in 1T-TaS_2. *Physical Review B* **49,** 16899–16916. doi:10.1103/PhysRevB.49.16899 (1994).

226. K. Sun, S. Sun, C. Zhu, et al. Hidden CDW states and insulator-to-metal transition after a pulsed femtosecond laser excitation in layered chalcogenide 1T-$TaS_{2-x}Se_x$. *Science Advances*. doi:10.1126/sciadv.aas9660 (2018).

227. D. Cho, S. Cheon, K.-S. Kim, et al. Nanoscale manipulation of the Mott insulating state coupled to charge order in 1T-TaS_2. *Nature Communications* **7,** 10453. doi:10.1038/ncomms10453 (2016).

228. A. W. Tsen, R. Hovden, D. Wang, et al. Structure and control of charge density waves in two-dimensional 1T-TaS_2. *Proceedings of the National Academy of Sciences* **112,** 15054–15059. doi:10.1073/pnas.1512092112 (2015).

229. S. Vogelgesang, G. Storeck, J. G. Horstmann, et al. Phase ordering of charge density waves traced by ultrafast low-energy electron diffraction. *Nature Physics* **14,** 184–190. doi:10.1038/nphys4309 (2018).

230. S. H. Sung, N. Schnitzer, S. Novakov, et al. Two-dimensional charge order stabilized in clean polytype heterostructures. *Nature Communications* **13,** 413. doi:10.1038/s41467-021-27947-5 (2022).

231. J.-P. v. Soest. *Optical and Electronic Reflectivity of TaS_2* BSc thesis (Leiden University, 2018). https://hdl.handle.net/1887/64692.

232. T. Iking. *Identifying TaS_2 polytypes in LEEM images using LEED simulations* BSc thesis (Leiden University, 2019). https://hdl.handle.net/1887/75227.

233. J. v. Landuyt, G. v. Tendeloo & S. Amelincky. Electron diffraction study of inter- and intrapolytypic phase transitions in transition metal dichalcogenides. I. Electron diffraction patterns. *physica status solidi (a)* **26,** 359–376. doi:10.1002/pssa.2210260138 (1974).

234. B. Burk, R. E. Thomson, A. Zettl & J. Clarke. Charge-density-wave domains in 1T-TaS_2 observed by satellite structure in scanning-tunneling-microscopy images. *Physical Review Letters* **66,** 3040–3043. doi:10.1103/PhysRevLett.66.3040 (1991).

235. K. Nakanishi, H. Takatera, Y. Yamada & H. Shiba. The Nearly Commensurate Phase and Effect of Harmonics on the Successive Phase Transition in 1T-TaS_2. *Journal of the Physical Society of Japan* **43,** 1509–1517. doi:10.1143/JPSJ.43.1509 (1977).

236. L. Ma, C. Ye, Y. Yu, et al. A metallic mosaic phase and the origin of Mott-insulating state in 1T-TaS2. *Nature Communications* **7,** 10956. doi:10.1038/ncomms10956 (2016).

237. L. Stojchevska, I. Vaskivskyi, T. Mertelj, et al. Ultrafast Switching to a Stable Hidden Quantum State in an Electronic Crystal. *Science* **344,** 177–180. doi:10.1126/science.1241591 (2014).

238. Q. Stahl, M. Kusch, F. Heinsch, et al. Collapse of layer dimerization in the photo-induced hidden state of 1T-TaS2. *Nature Communications* **11,** 1247. doi:10.1038/s41467-020-15079-1 (2020).